thermo

MDPI

Article

Analysis of Conductive Heat Transfer and Moisture Diffusion Through the Insulated Wall of a Refrigerated Warehouse

Laurențiu Mihail Constantin [1], Lavinia Grosu [2], Tiberiu Catalina [3,4], Adalia Andreea Percembli (Chelmuș) [1,*], Daniel Taban [1,*], Claudia Ioniță [1] and Alexandru Dobrovicescu [1]

[1] Department of Engineering Thermodynamics, Engines, Thermal and Refrigeration Equipment, National University of Science and Technology Politehnica București, 060042 Bucharest, Romania; ctinlaurentiumihail@gmail.com (L.M.C.); claudia.ionita@upb.ro (C.I.); adobrovicescu@upb.ro (A.D.)
[2] Laboratoire Energétique Mécanique Electromagnétisme (LEME), IUT de Ville d'Avray, 92410 Ville d'Avray, France; mgrosu@parisnanterre.fr
[3] Faculty of Building Services Engineering, Technical University of Civil Engineering, 020396 Bucharest, Romania; tiberiu.catalina@utcb.ro
[4] National Research and Development Institute URBAN-INCERC, 021652 Bucharest, Romania
* Correspondence: adalia.chelmus@stud.mec.upb.ro (A.A.P.); daniel.taban@upb.ro (D.T.)

Abstract

This study investigates steady-state conductive heat transfer and water-vapor diffusion through the external wall of a refrigerated warehouse with a specified load-bearing wall assembly. The formal analogy between heat conduction and mass diffusion is stated and used to establish a practical calculation framework for estimating heat and moisture ingress through multilayer cold-store walls. Calculation routines are presented to determine the temperature field and the corresponding water-vapor saturation and partial-pressure distributions across (and within) the insulation layer, enabling the identification of regions prone to interstitial condensation. The analysis highlights the roles of (i) the vapor diffusion resistance of the vapor barrier layer, (ii) the thermal resistance of the insulation, and (iii) key outdoor boundary conditions in governing condensation risk. Increasing insulation thermal resistance reduces external heat gains; however, it may also increase the likelihood of condensation in layers close to the cold side by lowering local temperatures and saturation pressures. Among external parameters, outdoor relative humidity exerts the strongest influence on interstitial condensation risk. For the investigated wall assembly, increasing outdoor relative humidity by 50% shifts the condensation onset location within the insulation toward mid-thickness. The effects of vapor barrier diffusion resistance, insulation thermal resistance, and changes in outdoor conditions (relative humidity, temperature, and wind speed) are reported in tabulated form and illustrated through pressure–position and temperature–position profiles.

Keywords: conductive heat transfer; moisture diffusion; refrigerated warehouse; wall insulation; steady-state analysis

Check for updates

Academic Editors: Sheng Xu and Johan Jacquemin

Received: 24 February 2026
Revised: 14 April 2026
Accepted: 16 April 2026
Published: 18 April 2026

Copyright: © 2026 by the authors. Licensee MDPI, Basel, Switzerland. This article is an open access article distributed under the terms and conditions of the Creative Commons Attribution (CC BY) license.

1. Introduction

The building sector is a major consumer of energy, with space heating and cooling representing a significant share of total demand [1,2]. The thermal performance of building insulation systems is a key factor in reducing energy consumption and greenhouse gas emissions in a built environment [3]. In practice, however, insulation materials are rarely maintained under perfectly dry conditions throughout their service life [4,5]. Moisture

ingress caused by mass diffusion, air leakage, construction moisture, or minor defects in the envelope components is often unavoidable and may persist for extended periods. Therefore, understanding the long-term impact of moisture on the thermal behavior of insulation systems is essential for reliable energy performance assessment and sustainable building design.

Conductive heat transfer and moisture through insulated walls have been extensively explored due to their critical role in maintaining thermal efficiency and preventing moisture-related damage. Previous research [6–8] highlights that the presence of moisture compromises thermal insulation not only by increasing its thermal conductivity (sensible effect), but also—more significantly—through the latent heat flux generated by evaporation and condensation, which may exceed the conductive heat flux. This dynamic demonstrates that heat and moisture transfer are inseparably coupled phenomena and cannot be analyzed in isolation. The critical influence of moisture content on the thermophysical properties of insulating materials was also quantified by Jerman and Černý [9], who show that the thermal conductivity of mineral wool can increase over fifteen-fold from dry to saturated states, whereas moisture diffusivity can vary by up to two orders of magnitude. Wang et al. [10] validate a coupled heat and moisture model, demonstrating a non-linear relationship in which the drying of a compromised insulation layer could temporarily improve its measured thermal resistance. This finding indicates that the effective thermal resistance of an insulation layer is not a fixed property, but a transient state dependent on its moisture content and the ongoing hygrothermal processes within the envelope.

The sensitivity of condensation risk to climatic boundary conditions was further emphasized by forward-looking analyses. A study applying the Glaser method to a wall assembly in a humid-temperate climate demonstrates that projected changes in atmospheric conditions—particularly increased volatility in monthly relative humidity—can introduce interstitial condensation risk, which has not been previously predicted under historical data [11]. Complementing material-level studies, a holistic assessment examined the building-scale energy impact of moisture in fiberglass insulation under hot humid conditions [12]. Laboratory measurements showed increased thermal conductivity with moisture content; however, whole-building energy simulations revealed that even moderately elevated moisture led to negligible changes in cooling energy demand, with less than 2% monthly variation. The study [12] concludes that the energy penalty from wet insulation is often moderated in practice by the composite behavior of the envelope assembly and the relatively small contribution of the wall transmission to the total cooling load. This underscores that while moisture degrades material properties, its system-level energy consequences are non-linear and climate-dependent. Nagy et al. [13] investigated the in situ degradation of mineral wool insulation extracted from a refurbished roof by comparing new, built-in, and severely degraded samples. The study identified a critical failure mode where "spoiled" samples, suffering from incomplete polymerization of the phenolic resin binder, underwent catastrophic compression (68% strain under load). This mechanical degradation reduced their effective thermal resistance by up to 40%, demonstrating that a latent material defect, activated by in-service moisture exposure, can lead to severe and coupled deterioration of both structural integrity and thermal performance. Investigations of advanced insulation materials have also been extended to aerogel-enhanced systems. One study prepared and characterized aerogel-enhanced plasters, blankets, and boards under a wide range of temperatures (–20 °C to +60 °C) and relative humidity levels (0–95% RH) [14]. The results quantify a strong hygric dependency: under 95% RH, the thermal conductivity of the aerogel gypsum board doubled, whereas the maximum temperature-driven increase was only 12%. This highlights that even for high-performance insulation,

the moisture content remains the primary environmental factor driving the degradation of the thermal resistance.

Because condensation-risk assessments rely on hygrothermal simulations, their credibility is fundamentally constrained by the quality of the input material properties. In addition, standardized estimation approaches are generally valid only within the hygroscopic range and can break down near saturation, where the vapor-phase transport dominates [15–17]. A study on hygroscopic insulation materials demonstrates that standard Heat Flow Meter (HFM) tests often require more than 160 h to reach full hygrothermal equilibrium [11]. If measurements are stopped prematurely, thermal conductivity may be overestimated by up to 40%, because latent heat associated with ongoing internal moisture redistribution is mistakenly recorded as conductive heat flow. This procedural artifact plausibly explains the pronounced scatter in the material property databases and indicates that revised testing durations are required for accurate characterization.

Another important perspective concerns economic and integrated performance. An optimization study by Zhang et al. [18] for a building located in a humid subtropical zone analyzes the life cycle performance and cost for five insulating materials with different thicknesses. This research highlights the critical concept of the "optimal economic thickness," representing a trade-off between initial investment and long-term energy savings. In the analyzed climate, increasing the insulation thickness reduces the heating load but may slightly increase the cooling load owing to the retention of internal heat during cool nights. These counterintuitive dynamics underscore the complexity of the coupling between the thermal properties of the building envelope and external climatic conditions, which directly influence the moisture balance and the interior surface temperature of the wall. Recent studies have extended this perspective to alternative wall configurations and efficient long-term numerical procedures for insulation design, including container-house wall systems and long-term simulations used for insulation thickness optimization [19,20].

In response to these challenges, contemporary research has increasingly focused on advanced numerical models based on Heat–Air–Moisture (HAM) theory. Tools such as Delphin [21] and WUFI [22] have been developed and widely adopted to capture these interactions under transient boundary conditions, providing valuable insight into long-term envelope performance [7,23–27]. Despite their advanced modeling capabilities, these hygrothermal simulation tools present notable limitations in engineering practice. The accuracy of their predictions is highly dependent on extensive material property data, careful calibration, significant computational effort, and advanced expertise for results interpretation [28]. This can limit their use in early-stage design or in contexts where rapid parametric evaluations are required. As a result, simplified methods continue to play an important role in preliminary assessments, regulatory compliance, normative relevance, and conceptual analysis [29,30]. Their applicability, however, is strongly dependent on the operating conditions of the building under consideration.

Refrigerated warehouses represent a specific class of buildings characterized by highly controlled and nearly constant indoor temperatures, large and persistent temperature gradients across the envelope, and relatively stable indoor humidity levels. Under these conditions, transient effects are reduced, and the envelope behavior may approach quasi-steady-state operation for extended periods. This operational regime creates a markedly different balance between thermal- and moisture-driving forces than that found in residential or office buildings. Therefore, in the present study, the wall is evaluated for representative operating states defined by fixed indoor setpoints and prescribed outdoor boundary conditions, rather than through time-varying climatic histories.

Despite the widespread use of cold storage facilities, the literature addressing moisture-related risks in their envelope systems remains limited, particularly with respect to analytical evaluation methods tailored to their unique operating regime.

In this context, the present study develops and applies a steady-state analytical framework for evaluating conductive heat transfer and water-vapor diffusion through the external walls of refrigerated warehouses. The formulation remains a one-dimensional steady-state heat-conduction and vapor-diffusion model and is evaluated through closed-form relations and layer-wise algebraic routines implemented in Engineering Equation Solver (EES) [31], with the corresponding calculation routines provided in Appendix A, Table A1. Its specific contribution lies in translating this steady-state heat-and-vapor-transfer framework into a practical calculation procedure for refrigerated wall assemblies, with evaluation of the temperature and water-vapor pressure fields both at wall interfaces and within the insulation layer for representative operating states. This enables a direct localization of the condensation-prone zone within the insulation thickness and supports a transparent parametric assessment of condensation sensitivity to insulation thermal resistance, vapor barrier diffusion resistance, and outdoor boundary conditions. The distinction of the present study therefore lies in how the steady-state framework is applied to multilayer refrigerated wall assemblies and used for parametric condensation risk evaluation, rather than in the introduction of new governing transport relations.

Rather than replacing advanced hygrothermal simulations, the proposed steady-state framework is intended as a physically transparent and computationally efficient tool for preliminary assessment and comparative analysis within its domain of validity.

The steady-state analysis presented in this study constitutes the first stage of a multi-step design methodology. After identifying the dominant transport mechanisms and selecting a preliminary wall configuration, the candidate solution can be further evaluated under dynamic boundary conditions using transient hygrothermal simulation tools, while accounting for climatic location, operating schedule, and wall orientation.

2. General Laws of Conductive Heat Transfer and Mass Diffusion

Conductive heat transfer and mass diffusion are governed by formally analogous transport laws.

2.1. Thermal Conduction

Consider a body in space (Figure 1), locally heated at a point P on an isothermal surface t. From point P, heat is transferred by conduction along the normal to the isothermal surface, in the direction of decreasing temperature.

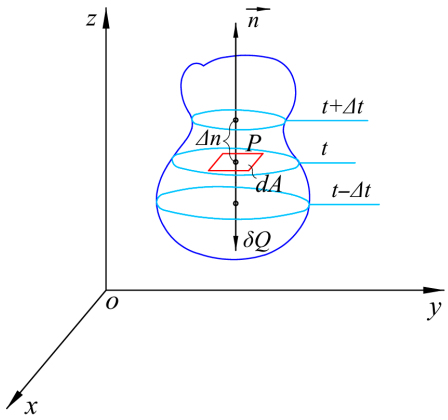


Figure 1. Heat transfer by thermal conduction along the normal to the surface, in the direction of decreasing temperature.

2.1.1. Fourier's Law

The differential amount of heat, δQ, that propagates by conduction is proportional to the temperature gradient, the differential area dA perpendicular to the direction of heat propagation, the time interval dτ during which heat is transferred, and a proportionality coefficient k that characterizes the material's ability to conduct heat, called thermal conductivity:

$$\delta Q = -k\frac{\partial t}{\partial n} dA \cdot d\tau \ [J] \ . \tag{1}$$

The specific (unit) heat flux is defined as the amount of heat transferred by conduction per unit time through a unit area normal to the direction of the heat transfer:

$$q = \frac{\delta Q}{dA} = -k\frac{\partial t}{\partial n} \left[\frac{W}{m^2}\right]. \tag{2}$$

Thermal conductivity represents the amount of heat transferred by conduction per unit time through a unit area for a unit temperature gradient (1[K] per unit length)

$$k = \frac{q}{-\frac{\partial t}{\partial n}} \left[\frac{\frac{W}{m^2}}{\frac{K}{m}} = \frac{W}{m \cdot K}\right]. \tag{3}$$

2.1.2. Fourier Differential Equation (Without Internal Heat Sources)

During conductive heat transfer, the temperature within the body varies with the spatial coordinates and time, $t = t(x, y, z, \tau)$

$$\frac{\partial t}{\partial \tau} = a\left(\frac{\partial^2 t}{\partial x^2} + \frac{\partial^2 t}{\partial y^2} + \frac{\partial^2 t}{\partial z^2}\right), \tag{4}$$

where

$$a = \frac{k}{\rho \cdot c_p} \left[\frac{m^2}{s}\right], \tag{5}$$

is the thermal diffusivity of the material through which heat propagates.

2.2. Mass Diffusion

Consider a body in space characterized by isothermal surfaces, whose temperatures decrease along the direction of conductive heat flux (Figure 2).

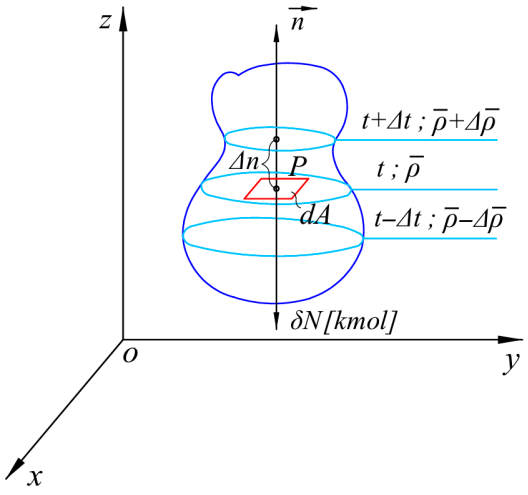


Figure 2. Molar diffusion along the normal to the surface, in the direction of decreasing density.

The conductive heat flux is accompanied by a diffusive mass flux that occurs in the direction of decreasing density.

The direction of the surface normal corresponds to increasing density (Figure 2), and the rate of density change along the normal direction per unit length is called a density gradient.

In the case of molar diffusion, where the overbar denotes molar quantities, one distinguishes:

(a) molar density gradient

$$\text{grad}\,\overline{\rho} = \lim\left(\frac{\Delta\overline{\rho}}{\Delta n}\right)_{\Delta n\to 0} = \frac{\partial\overline{\rho}}{\partial n}\left[\frac{\text{kmol}}{\text{m}^4}\right], \tag{6}$$

and correspondingly,

(b) molar density drop

$$-\text{grad}\,\overline{\rho} = -\frac{\partial\overline{\rho}}{\partial n}\left[\frac{\text{kmol}}{\text{m}^4}\right] \tag{7}$$

Diffusive mass transfer arises from the random motion of particles of a given substance through a medium, owing to a concentration gradient.

Mass transfer characterizes mixtures with two or more components, such as moist air, which is considered a mixture of dry air and water vapor. The specific properties of each component, or the average properties of the mixture, can be expressed on a mass or molar basis.

Consider a gaseous mixture of ideal gases.

For molar averaging, the amount of substance measured in kmol is:

$$N = \Sigma N_i\,. \tag{8}$$

The molar density of a component i is denoted as:

$$\overline{\rho}_i = \frac{N_i}{V} = \frac{m_i}{M_i}\cdot\frac{1}{V} = \frac{\rho_i}{M_i}\left[\frac{\text{kmol}}{\text{m}^3}\right]. \tag{9}$$

The mean molar density of the mixture can be written as follows:

$$\overline{\rho} = \frac{N}{V} = \frac{\Sigma N_i}{V} = \sum_{i=1}^{n}\overline{\rho}_i\,. \tag{10}$$

The molar composition of the mixture is expressed in terms of mole concentrations:

$$\overline{c}_i = \frac{N_i}{N}. \tag{11}$$

From relations (9)–(11) it follows that:

$$\overline{c}_i = \frac{\overline{\rho}_i}{\overline{\rho}}\,. \tag{12}$$

Assume that each component i moves in the mixture with a different velocity $w_i\left[\frac{m}{s}\right]$, corresponding to a different molar flux $\overline{G}_i$.

The concept of unit molar flux is introduced as the molar flow rate per unit area:

$$\overline{G} = \left[\frac{\text{kmol}}{\text{s}\cdot\text{m}^2}\right] = \overline{\rho}\left[\frac{\text{kmol}}{\text{m}^3}\right]\cdot w\left[\frac{\text{m}}{\text{s}}\right] = \Sigma(\overline{\rho}_i\cdot w_i) = \Sigma\overline{G}_i\,. \tag{13}$$

https://doi.org/10.3390/thermo6020027

The mean mixture velocity can be defined as:

$$w\left[\frac{m}{s}\right] = \frac{1}{\overline{\rho}}\sum_{i=1}^{n}(\overline{\rho}_i \cdot w_i) = \Sigma \overline{c}_i \cdot w_i. \tag{14}$$

The difference $(w_i - w)$ is called the diffusion velocity of component i, and

$$\overline{J}_i = \overline{\rho}_i(w_i - w)\left[\frac{kmol}{m^2 \cdot s}\right], \tag{15}$$

is the unit molar diffusion flux of component i (or the molar diffusion velocity).

2.2.1. Fick's First Law (Steady-State Diffusion)

The differential molar amount of substance, δN, transferred by diffusion is proportional to the molar density drop, the differential area dA normal to the diffusion direction, the time interval dτ, and a proportionality coefficient D, which characterizes the medium's ability to allow diffusion and is called the molar diffusivity coefficient [32]:

$$\delta N = -D\frac{\partial \overline{\rho}}{\partial n} dA \cdot d\tau \ [kmol]. \tag{16}$$

The unit molar diffusion flux, also referred to as the molar diffusion velocity, is defined as the amount of substance, in kmol, transferred by diffusion per unit time through a unit area perpendicular to the diffusion direction:

$$\overline{J} = \frac{\delta \dot{N}}{dA} = -D\frac{\partial \overline{\rho}}{\partial n}\left[\frac{kmol}{s \cdot m^2}\right]. \tag{17}$$

The molar diffusivity D is the amount of substance, in kmol, that diffuses per unit time through a unit area under unit molar density gradient of 1 [kmol/m^3] per unit length:

$$D = \frac{\overline{J}}{-\frac{\partial \overline{\rho}}{\partial n}}\left[\frac{kmol}{s \cdot m^2} \cdot \frac{m}{\frac{kmol}{m^3}} = \frac{m^2}{s}\right]. \tag{18}$$

For a component A of an ideal gas mixture diffusing through a medium B, relations (15) and (17) can be expressed as follows:

$$\overline{J}_A = \overline{\rho}_A \cdot (w_A - w) = -D_{AB}\frac{\partial \overline{\rho}_A}{\partial n}. \tag{19}$$

Noting that:

$$\overline{\rho}_A = \overline{c}_A \cdot \overline{\rho}, \tag{20}$$

where $\overline{\rho}$ is the molar density of the mixture. Substituting into (19) yields:

$$\overline{J}_A = \overline{\rho}_A(w_A - w) = -\overline{\rho} \cdot D_{AB}\frac{\partial \overline{c}_A}{\partial n}. \tag{21}$$

If mass transfer is multidirectional, Equation (21) can be written as:

$$\overline{J}_A = \overline{\rho}_A(w_A - w) = -\overline{\rho} \cdot D_{AB} \cdot \nabla \overline{c}_A, \tag{22}$$

where

$$\nabla \overline{c}_A = \frac{\partial \overline{c}_A}{\partial x} + \frac{\partial \overline{c}_A}{\partial y} + \frac{\partial \overline{c}_A}{\partial z}. \tag{23}$$

2.2.2. Fick's Second Law (Unsteady Diffusion)

If the molar density of component A depends on both the spatial coordinates and time $\bar{\rho}_A(x, y, z, \tau)$, the molar diffusion differential equation can be written as

$$\frac{\partial \bar{\rho}_A}{\partial \tau} = D_{AB}\left(\frac{\partial^2 \bar{\rho}_A}{\partial x^2} + \frac{\partial^2 \bar{\rho}_A}{\partial y^2} + \frac{\partial^2 \bar{\rho}_A}{\partial z^2}\right). \quad (24)$$

Considering Equation (12), relation (24) can be expressed as

$$\frac{\partial \bar{c}_A}{\partial \tau} = D_{AB}\left(\frac{\partial^2 \bar{c}_A}{\partial x^2} + \frac{\partial^2 \bar{c}_A}{\partial y^2} + \frac{\partial^2 \bar{c}_A}{\partial z^2}\right). \quad (25)$$

3. Analytical Expressions for the Unit Fluxes

3.1. Thermal Conduction Through a Homogeneous Plane Wall

To derive the finite expression for the unit heat flux (Equation (2)), Fourier differential equation (Equation (4)) is applied to a steady-state, one-dimensional process (along the x-direction) for a homogeneous plane wall, as shown in Figure 3.

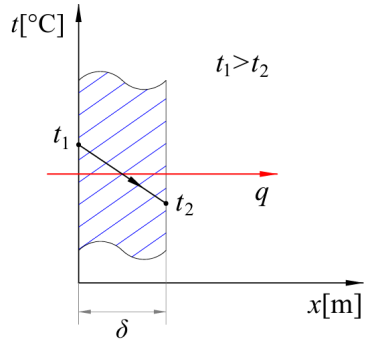


Figure 3. Schematic representation of one-dimensional steady conductive heat transfer through a homogeneous plane wall of thickness δ, with boundary temperatures t_1, t_2 and heat flux q along the x-direction.

Integration of the steady-state Fourier differential equation (Equation (4)) gives:

$$q = \frac{t_1 - t_2}{\frac{\delta}{k}} = \frac{t_1 - t_2}{R_t^{cond}}. \quad (26)$$

3.2. Mass Diffusion

To obtain the finite form of the unit molar diffusion flux (Equation (21)), Equation (25) is applied to the steady-state, one-dimensional diffusion process as illustrated in Figure 4.

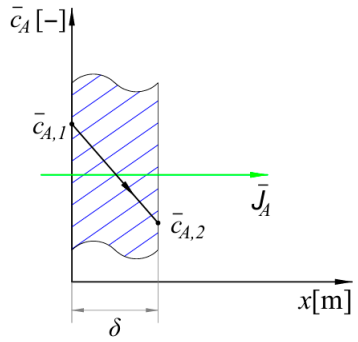


Figure 4. Schematic representation of one-dimensional steady molar diffusion of component A through a plane wall of thickness δ, with boundary mole fractions $c_{A,1}$, $c_{A,2}$ and diffusion flux J_A along the x-direction.

Integration of the steady-state Fick's Second Law (Equation (25)) gives:

$$\bar{J}_A = -\bar{\rho}\cdot D_{AB}\frac{\bar{c}_{A,2}-\bar{c}_{A,1}}{\delta} = \frac{\bar{c}_{A,1}-\bar{c}_{A,2}}{\frac{\delta}{\bar{\rho}\cdot D_{AB}}} = \frac{\bar{c}_{A,1}-\bar{c}_{A,2}}{R_D^{mol}}, \quad (27)$$

where the molar diffusion resistance is

$$R_D^{mol} = \frac{\delta[m]}{\bar{\rho}\left[\frac{kmol}{m^3}\right]\cdot D_{AB}\left[\frac{m^2}{s}\right]}\left[\frac{m^2\cdot s}{kmol}\right], \quad (28)$$

with $\bar{\rho}$ representing the molar density of the mixture formed by components A and B.

A dimensional analysis confirms the correctness of this result:

$$\bar{J}_A\left[\frac{kmol\ A}{m^2 s}\right]\ (\text{molar velocity or unit molar diffusion flux of component A}) = \frac{\bar{c}_{A,1}-\bar{c}_{A,2}[-]}{R_D^{mol}\left[\frac{m^2\cdot s}{kmol}\right]}.$$

4. Application—Moisture Diffusion from Moist Air Through a Plane Wall

In this case, the thermodynamic driving force for diffusion is the drop in the molar concentration of water vapor, ultimately leading to a drop in the partial pressure p_v of water vapor in moist air across the wall faces, along the direction of moisture transfer. For moist air treated as an ideal gas at uniform total pressure, this formulation is equivalent to expressing the driving force directly as the gradient of p_v, and it refers strictly to diffusive transport, without accounting for pressure-driven convective flow.

The expression for the unit molar diffusion flux (or molar diffusion velocity) (Equation (27)) is used, where the mole concentration of water vapor $\bar{c}_{A,1}$ and $\bar{c}_{A,2}$ on the two wall faces (in the direction of decreasing temperature) is given by:

$$\bar{c}_{A,1} = \frac{p_{v,1}}{p} \text{ and } \bar{c}_{A,2} = \frac{p_{v,2}}{p}, \quad (29)$$

where component A is represented by water vapor, and p is the pressure of moist air (atmospheric pressure).

Substituting relation (29) into relation (27) yields:

$$\bar{J}_v = \frac{\frac{p_{v_1}}{p}-\frac{p_{v_2}}{p}}{\frac{\delta}{\bar{\rho}_{ma}\cdot D_{vw}}} = \frac{p_{v,1}-p_{v,2}}{\frac{p\cdot\delta}{\bar{\rho}_{ma}\cdot D_{vw}}}\left[\frac{kmol\ v}{m^2\cdot s}\right], \quad (30)$$

where $\bar{J}_v$ is the molar diffusion flux of water vapor through wall w, $\bar{\rho}_{ma}$ is the molar density of moist air (a mixture of water vapor and dry air), and D_{vw} is the diffusion coefficient of water vapor through wall w.

A dimensional check confirms the correctness of the relation

$$\bar{J}_v\left[\frac{kmol}{m^2\cdot s}\right] = \frac{\left(p_{v,1}-p_{v,2}\right)[Pa]}{\frac{p[Pa]\cdot\delta[m]}{\bar{\rho}_{ma}\left[\frac{kmol}{m^3}\right]\cdot D_{vw}\left[\frac{m^2}{s}\right]}} = \left[\frac{kmol}{m^2\cdot s}\right].$$

The wall molar permeability coefficient for water vapor can be defined as

$$\frac{\bar{\rho}_{ma}\cdot D_{vw}}{p} = \bar{\mu}\left[\frac{\frac{kmol}{m^3}\cdot\frac{m^2}{s}}{Pa} = \frac{kmol\ ma}{m\cdot s\cdot Pa}\right], \quad (31)$$

and represents the amount of moist air (in kmol) that permeates a wall of unit surface area and unit thickness per unit time, driven by a unit difference in water vapor partial pressure between the two faces of the wall.

Substituting Equation (31), Equation (30) can be written as:

$$\bar{J}_v = \frac{P_{v,1} - P_{v,2}}{\frac{\delta}{\bar{\mu}}} \left[\frac{\text{kmol v}}{m^2 \cdot s}\right]. \quad (32)$$

By extending the analytical reasoning developed for heat conduction through a plane wall to molar mass transfer, the formal analogy between the two transport processes is highlighted, as shown in Table 1.

Table 1. Similarity analysis between heat conduction and mass diffusion.

Thermal Conduction	Mass Diffusion
Temperature gradient $-\frac{dt}{dx}\left[\frac{K}{m}\right]$	Water-vapor concentration * gradient (molar concentration difference) $-\frac{dp_v}{dx}\left[\frac{Pa}{m}\right]$
Unit heat flux $q = -k\frac{dt}{dx}\left[\frac{W}{m^2}\right]$	Unit molar mass flux $\bar{J}_v = -\bar{\mu}\frac{dp_v}{dx}\left[\frac{kmol}{m^2 \cdot s}\right]$
Thermal conductivity coefficient $k\left[\frac{W}{m \cdot K}\right]$	Molar permeability coefficient $\bar{\mu}\left[\frac{kmol}{s \cdot m \cdot Pa}\right]$
Thermal diffusivity coefficient $a\left[\frac{m^2}{s}\right]$	Molar diffusivity coefficient $D\left[\frac{m^2}{s}\right]$
Conductive thermal resistance $R_t = \frac{\delta}{k}\left[\frac{m^2 \cdot K}{W}\right]$	Molar diffusion resistance $R_D = \frac{\delta}{\bar{\mu}}\left[\frac{m^2 \cdot Pa \cdot s}{kmol}\right]$

* Equivalently expressed as a partial-pressure gradient under the ideal-gas assumption.

5. Design Calculation of the Refrigerated Warehouse Wall Insulation

The analysis considers the external wall of a refrigerated warehouse with a defined load-bearing structure as shown schematically in Figure 5.

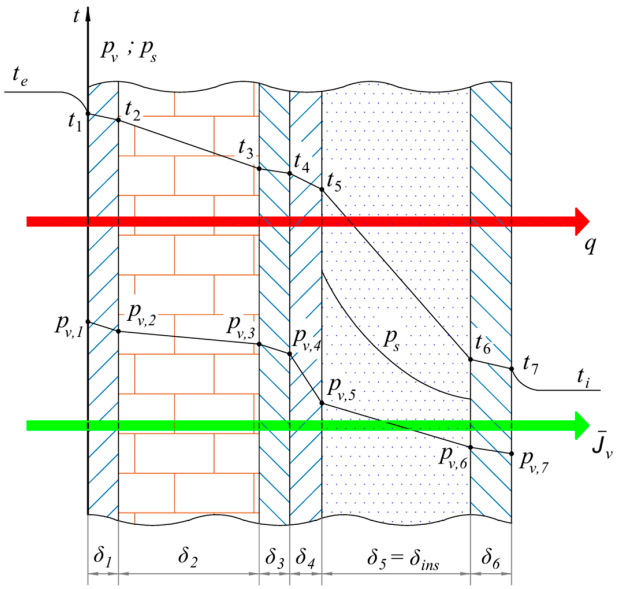


Figure 5. Layered structure of the composite external wall.

The wall assembly comprises six layers, each characterized by its thickness δ_j, thermal conductivity k_j, and molar permeability $\overline{\mu}_j$, arranged from the exterior (warm) side to the interior (cold) side, as follows:

- exterior plaster (render) $(\delta_1, k_1, \overline{\mu}_1)$;
- expanded concrete masonry $(\delta_2, k_2, \overline{\mu}_2)$;
- base coat plaster (cement mortar) $(\delta_3, k_3, \overline{\mu}_3)$;
- vapor barrier $(\delta_4, k_4, \overline{\mu}_4)$;
- insulation $(\delta_5, k_5, \overline{\mu}_5)$;
- finishing plaster $(\delta_6, k_6, \overline{\mu}_6)$.

Heat ingress from the outdoor environment toward the refrigerated space occurs by convection at the exterior and interior wall surfaces, and by conduction through the wall layers. The overall heat transfer coefficient is calculated as follows:

$$U = \frac{1}{\frac{1}{h_e} + \sum\left(\frac{\delta}{k}\right)_j + \left(\frac{\delta}{k}\right)_{ins} + \frac{1}{h_i}}, \; j \in \{1, 2, 3, 4, 6\}. \tag{33}$$

Radiative heat transfer at the exterior and interior wall surfaces is not modeled explicitly in the present study—the surface terms h_e and h_i therefore represent only convective heat transfer coefficients.

For a prescribed design value of the overall heat transfer coefficient U, the required insulation thermal resistance R_t^{ins} is:

$$R_t^{ins} = \left(\frac{\delta}{k}\right)_{ins} = \frac{1}{U} - \left(\frac{1}{h_e} + \sum\left(\frac{\delta}{k}\right)_j + \frac{1}{h_i}\right), \tag{34}$$

where $\sum\left(\frac{\delta}{k}\right)_j$ represents the sum of the conductive thermal resistances of the load-bearing layers, excluding the insulation layer.

For the north-facing external wall under consideration, the assembly comprises five structural/insulating layers with specified materials and thicknesses, in addition to a vapor barrier layer. The vapor barrier is positioned on the outdoor side of the insulation and is intended to limit moisture ingress, thereby reducing the risk of interstitial condensation within the insulation.

The mathematical model accounts for both heat transfer and water-vapor diffusion from the outdoor air to the controlled indoor atmosphere of the refrigerated warehouse (t_i, φ_i, h_i), which is maintained by the refrigeration system.

By analyzing the convective heat transfer at the exterior and interior wall surfaces, together with the conductive transfer through the multilayer wall, it is possible to determine the temperature profile across each layer and the corresponding water-vapor saturation pressure profile based on the local wall temperature.

By selecting the overall heat transfer coefficient $U\left[\frac{W}{m^2 \cdot K}\right]$ and specifying the outdoor temperature t_e and refrigerated space temperature t_i, the unit heat flux entering the refrigerated space can be determined as:

$$q = U(t_e - t_i) \quad \left[\frac{W}{m^2}\right]. \tag{35}$$

Given the unit heat flux q, the convective heat transfer coefficients h_e and h_i, the thickness δ and thermal conductivity k of each wall layer, the temperatures at the external and internal faces of each layer (inter-layer temperatures) can be calculated.

For instance, at the warm (external) face of the insulation (Figure 5):

$$t_5 = t_e - q\left(\frac{1}{h_e} + \frac{\delta_1}{k_1} + \frac{\delta_2}{k_2} + \frac{\delta_3}{k_3} + \frac{\delta_4}{k_4}\right) = t_e - q\left(\frac{1}{h_e} + \sum_{j=1}^{4}\left(\frac{\delta}{k}\right)_j\right). \quad (36)$$

Noting that the temperature profile for conductive heat transfer normal to a plane wall is linear, temperatures within each wall layer (intra-layer temperatures) can also be determined.

Simultaneously with heat transfer, water-vapor diffusion occurs through the wall layers. Given the temperature profile, the local saturation pressure $p_s(T)$ of water vapor can be evaluated both at the interfaces and within the layers.

The unit molar flux of water vapor, $\bar{J}_v$, diffusing through the wall is calculated as follows:

$$\bar{J}_v = \frac{p_{v_e} - p_{v_i}}{\frac{\delta_1}{\bar{\mu}_1} + \frac{\delta_2}{\bar{\mu}_2} + \frac{\delta_3}{\bar{\mu}_3} + \frac{\delta_4}{\bar{\mu}_4} + \frac{\delta_5}{\bar{\mu}_5} + \frac{\delta_6}{\bar{\mu}_6}} = \frac{p_{v_e} - p_{v_i}}{\sum_{j=1}^{6}\left(\frac{\delta}{\bar{\mu}}\right)_j} = \frac{p_{v_e} - p_{v_i}}{\sum_{j=1}^{6} R_j^{dif}}. \quad (37)$$

Neglecting convective thermal resistance at the external and interior faces of the composite wall, the water-vapor partial pressures at the two boundary surfaces are given by

$$p_{v_e} = \varphi_e \cdot p_{s_e}, \quad (38)$$

$$p_{v_i} = \varphi_i \cdot p_{s_i}. \quad (39)$$

Since the unit molar water-vapor flux $\bar{J}_v$ is constant across all wall layers under steady-state conditions, the corresponding partial pressures p_v can be determined at any interface between layers (inter-layer) or within any layer (intra-layer). For example, at the warm face of the insulation layer (Figure 5)

$$p_{v_5} = p_{v_e} - \bar{J}_v\left(\frac{\delta_1}{\bar{\mu}_1} + \frac{\delta_2}{\bar{\mu}_2} + \frac{\delta_3}{\bar{\mu}_3} + \frac{\delta_4}{\bar{\mu}_4}\right) = p_{v_e} - \bar{J}_v\sum_{j=1}^{4}\left(\frac{\delta}{\bar{\mu}}\right)_j. \quad (40)$$

In the analysis, the material properties of the wall layers are considered constant, although in practice they may depend on temperature and moisture content. Consequently, the calculated temperature field and the corresponding saturation and water-vapor partial-pressure profiles refer to the prescribed steady-state operating conditions and the adopted layer properties.

The temperature field and the saturation and water-vapor partial pressures profiles were computed using EES [31].

Analysis of the relative positions of the saturation pressure curve p_s and the water-vapor partial pressure curve p_v at a given temperature indicates the possibility of condensation occurring in the considered layer (Figure 6).

In Figure 6, the saturation pressure profile p_s at a given temperature and the water-vapor partial pressure profiles p_v, determined from temperature and humidity, are shown on a T–s diagram.

At a given location, comparing the saturation pressure $p_s(T)$ with the vapor partial pressure p_v indicates whether condensation is possible. Where $p_v < p_s$, vapor remains in the gaseous state; where $p_v > p_s$, interstitial condensation can occur. In cold-store walls, condensation risk is typically highest within or near the insulation because, due to its function and material properties, insulation produces a steep temperature drop, causing a sharp decrease in p_s that may fall below p_v, thereby initiating condensation.

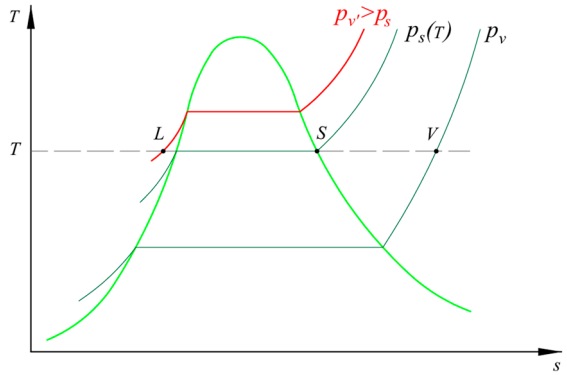


Figure 6. Representation of the saturation pressure p_s at a given temperature T along with several water-vapor partial pressures on a T–s diagram.

6. Influence of External Environmental Factors on the Risk of Condensation in the Refrigerated Warehouse Wall Insulation

This section investigates how, for a given thickness of the vapor barrier layer, variations in outdoor climatic conditions can lead to condensation within the insulation layer.

The considered outdoor climatic parameters include relative humidity φ_e, temperature t_e, and wind speed at the wall surface, the latter being represented by the convective heat transfer coefficient h_e, which characterizes convective heat transfer at the interface between the wall and the moving outdoor air.

The structural characteristics of the multilayer wall (Figure 5) are summarized in Table 2 [33].

Table 2. Structural characteristics of the layers of the composite wall.

Layer	Material Layers	Thickness δ [m]	Thermal Conductivity Coefficient k $\left[\frac{W}{m \cdot K}\right]$	Molar Permeability Coefficient $\overline{\mu}$ $\left[\frac{kmol}{m \cdot s \cdot Pa}\right]$
1	exterior plaster (render)	0.03	1	7.18×10^{-13}
2	expanded concrete masonry	0.25	0.4	9.34×10^{-13}
3	base coat plaster (cement mortar)	0.03	1.16	7.18×10^{-13}
4	vapor barrier	variable	0.348	8.23×10^{-15}
5	insulation	variable	0.04	2.15×10^{-13}
6	finishing plaster	0.03	1.16	7.18×10^{-13}

6.1. Effect of Outdoor Relative Humidity

The analysis was performed for $\delta_{ins} = 0.14$ m ($U = 0.23 \frac{W}{m^2 \cdot K}$, $h_e = 25 \frac{W}{m^2 \cdot K}$, $t_e = 30\ ^\circ C$), and for various vapor barrier thicknesses.

As shown in Figure 7, the saturation pressure dropped below the water-vapor pressure, indicating the onset of condensation within the mid-thickness region of the insulation at $\varphi_e = 0.6$. As the external relative humidity φ_e increased, the condensation zone progressively shifted toward the warm surface of the insulation.

For the specified layer materials of the multilayer wall and the selected vapor barrier material (Table 2), a vapor-barrier thickness of $\delta_4 = 4$ mm did not prevent condensation formation, even in a relatively dry outdoor environment with $\varphi_e = 0.6$.

As the vapor barrier thickness increased (Figures 8–10), the location where condensation occurred shifted further from the entry, following the direction of heat and mass transfer, for the same φ_e. For a given vapor-barrier thickness δ_4, an increase in the outdoor relative humidity shifts the condensation risk toward the warm face of the insulation.

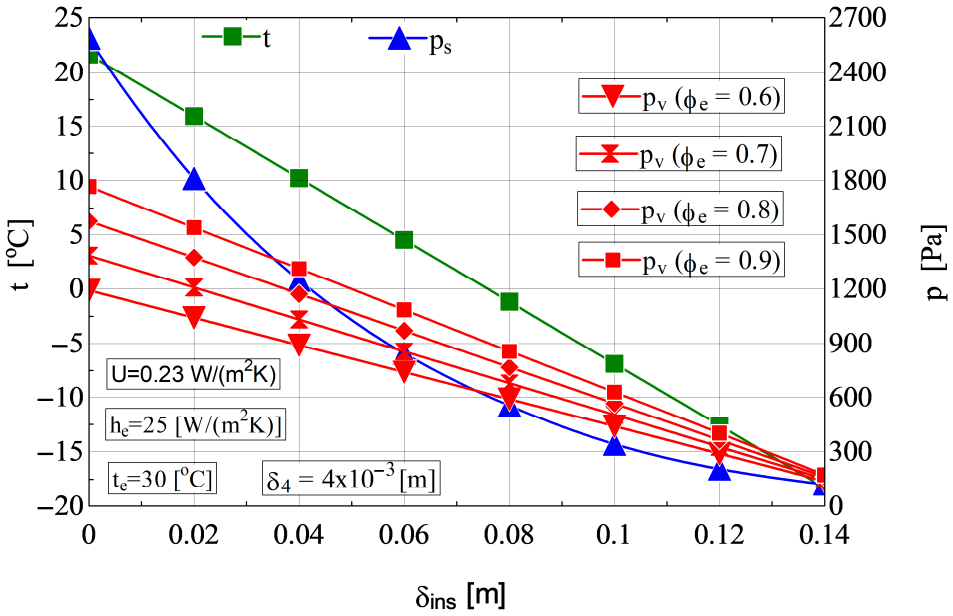


Figure 7. Variation in temperature, saturation pressure (p_s), and water-vapor partial pressure (p_v) within the insulation layer of $\delta_{ins} = 140$ mm, for a vapor barrier layer of $\delta_4 = 4$ mm, under varying external air relative humidity φ_e.

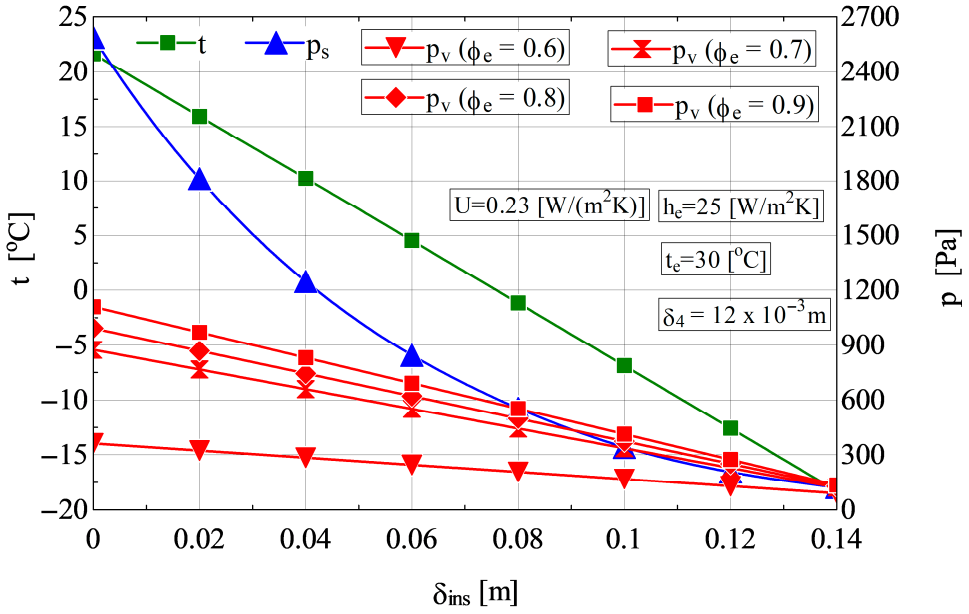


Figure 8. Variation in temperature, saturation pressure (p_s), and water-vapor partial pressure (p_v) within the insulation layer of $\delta_{ins} = 140$ mm, for a vapor barrier layer of $\delta_4 = 12$ mm, under varying external air relative humidity φ_e.

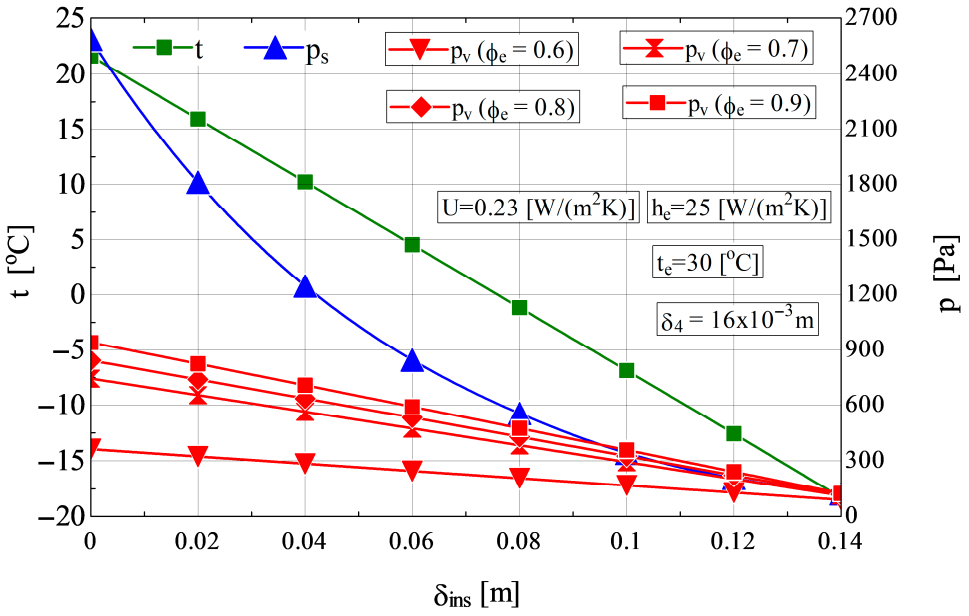


Figure 9. Variation in temperature, saturation pressure (p_s), and water-vapor partial pressure (p_v) within the insulation layer of $\delta_{ins} = 140$ mm, for a vapor barrier layer of $\delta_4 = 16$ mm, under varying external air relative humidity φ_e.

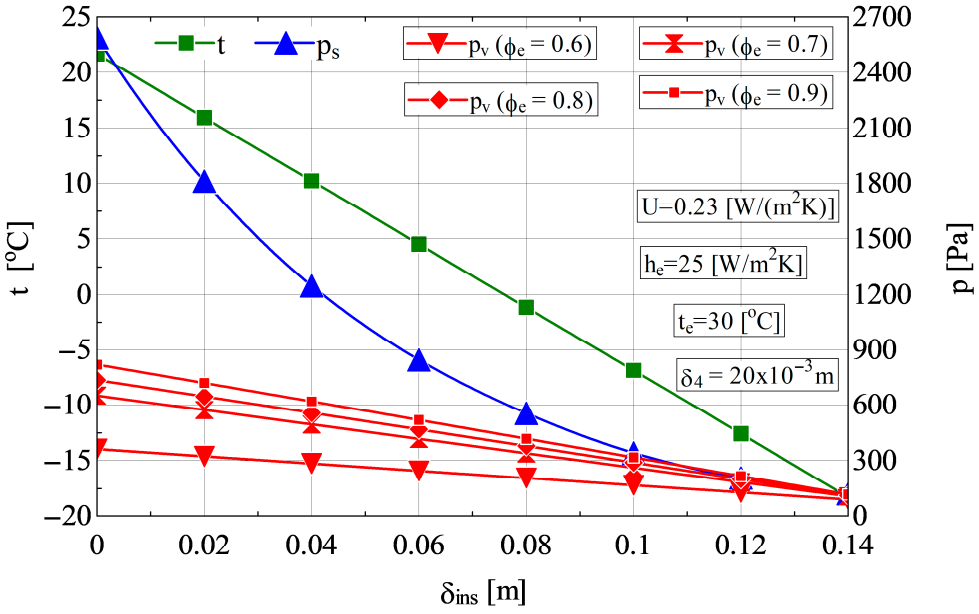


Figure 10. Variation in temperature, saturation pressure (p_s), and water-vapor partial pressure (p_v) within the insulation layer of $\delta_{ins} = 140$ mm, for a vapor barrier layer of $\delta_4 = 20$ mm, under varying external air relative humidity φ_e.

Under the specified outdoor conditions and for an insulation thickness of $\delta_{ins} = 140$ mm, only a vapor barrier thickness of $\delta_4 = 24$ mm prevents the risk of condensation, even at a high outdoor relative humidity $(\varphi_e = 0.9)$ (Figure 11).

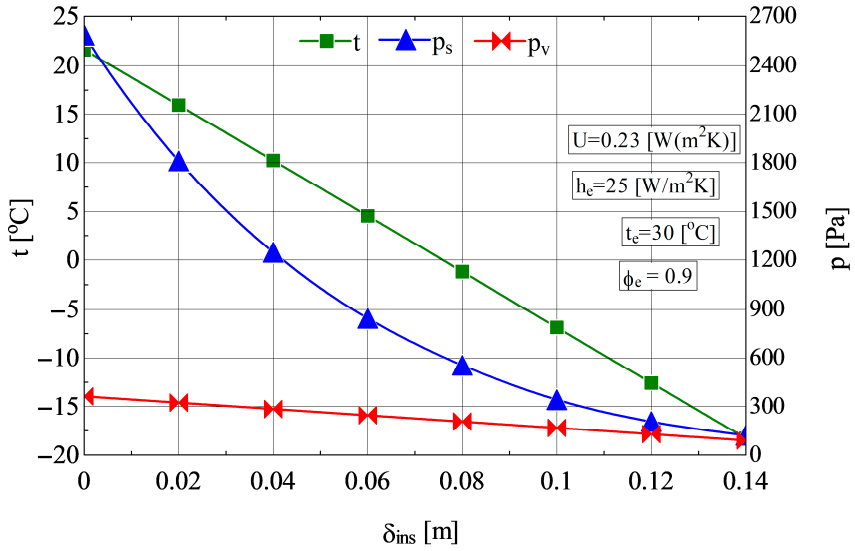


Figure 11. Variation in temperature, saturation pressure (p_s), and water-vapor partial pressure (p_v) within the insulation layer of $\delta_{ins} = 140$ mm, for a vapor barrier layer of $\delta_4 = 24$ mm, under varying external air relative humidity φ_e.

6.2. Influence of Insulation Thickness on Condensation Risk

Increasing the insulation thickness lowers the temperature of the cold-side surface of the insulation, approaching the refrigerated space temperature (t_i). Consequently, the risk of condensation near the cold surface increases. To prevent condensation, a vapor barrier with lower moisture permeability or greater thickness is required. Although these are more expensive construction solutions, a higher initial investment could be offset by operational energy savings.

For a thinner insulation layer $\left(\delta_{ins} = 100 \text{ mm}, U = 30\frac{W}{m^2K}\right)$, the analysis of different vapor barrier thicknesses and outdoor relative humidity indicates that a vapor barrier thickness of $\delta_4 = 20$ mm effectively prevents condensation, even under high external humidity ($\varphi_e = 0.9$) (Figure 12).

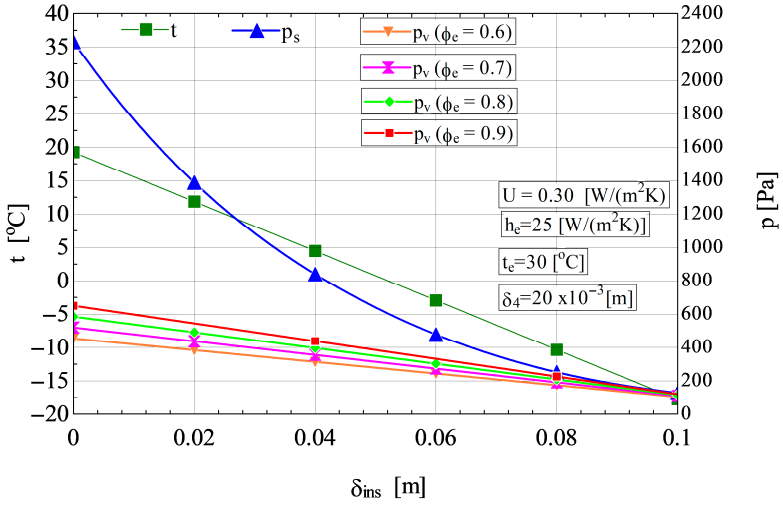


Figure 12. Variation in temperature, saturation pressure (p_s), and water-vapor partial pressure (p_v) within the insulation layer of $\delta_{ins} = 100$ mm, for a vapor barrier layer of $\delta_4 = 20$ mm, under varying external air relative humidity φ_e.

6.3. Outdoor Temperature Influence on Condensation Risk

A case study was performed for an insulation layer thickness of $\delta_{ins} = 100$ mm, a vapor barrier thickness of $\delta_4 = 16$ mm, and outdoor relative humidity of $\varphi_e = 0.85$.

Figures 13–15 show that an increase in the outdoor temperature (t_e) increases the risk of condensation, particularly at high external temperatures. Both the saturation pressure and the water-vapor partial pressure within the insulation increased with increasing outdoor temperature. However, because p_v rises more rapidly than p_s in the colder layers, the vapor pressure exceeds the local saturation pressure, leading to condensation.

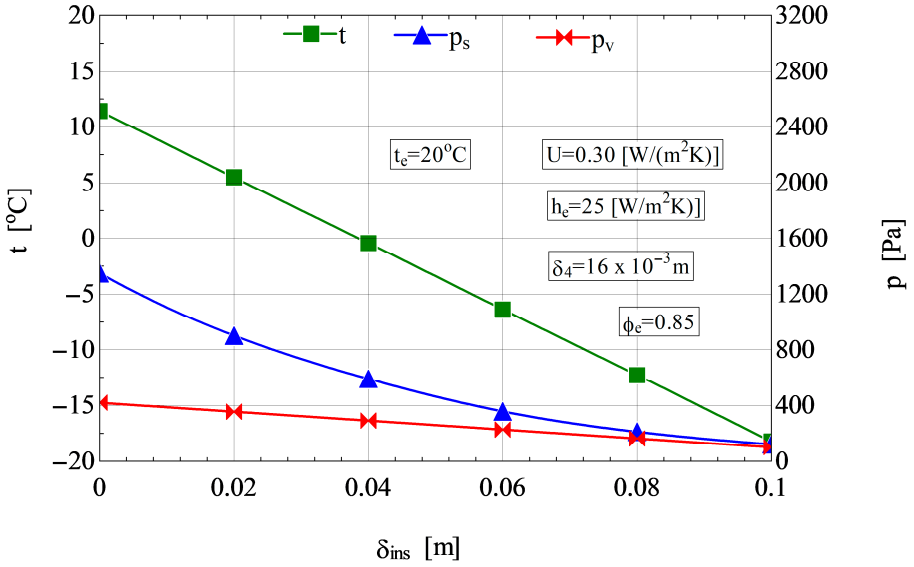


Figure 13. Variation in temperature, saturation pressure (p_s), and water-vapor partial pressure (p_v) within the insulation layer of $\delta_{ins} = 100$ mm, for a vapor barrier layer of $\delta_4 = 16$ mm, and an external air temperature of $t_e = 20$ °C.

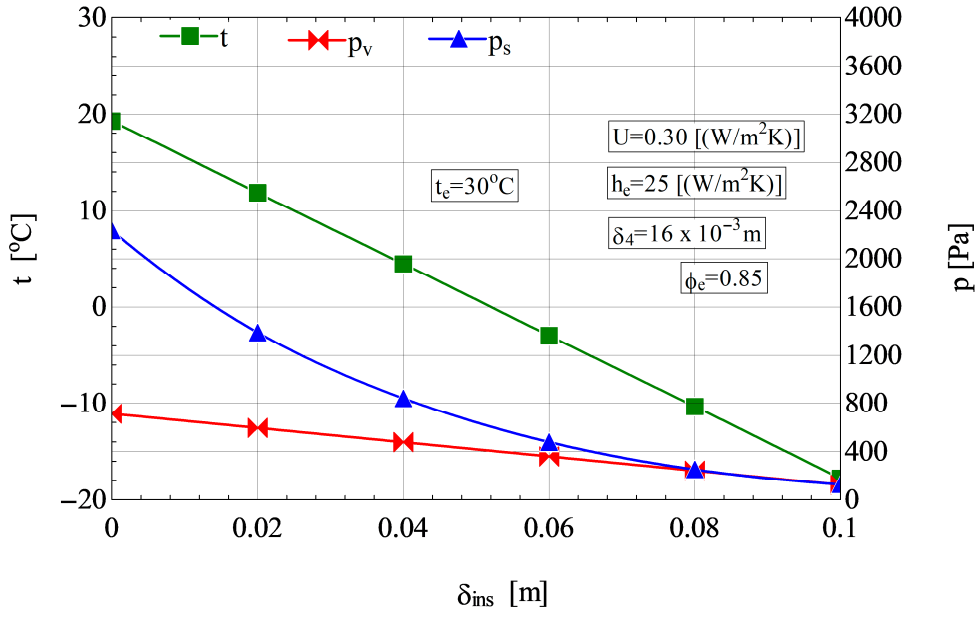


Figure 14. Variation in temperature, saturation pressure (p_s), and water-vapor partial pressure (p_v) within the insulation layer of $\delta_{ins} = 100$ mm, for a vapor barrier layer of $\delta_4 = 16$ mm, and an external air temperature of $t_e = 30$ °C.

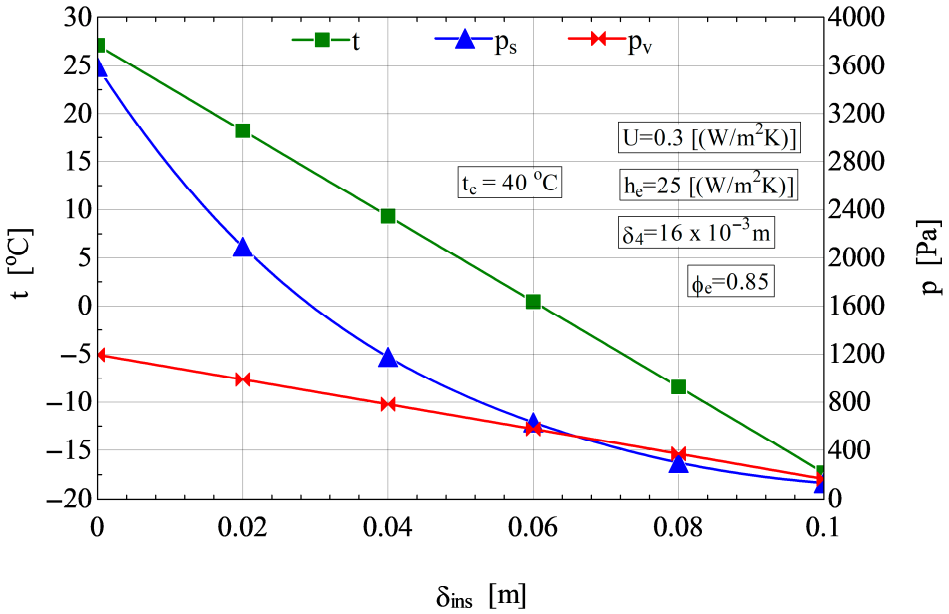


Figure 15. Variation in temperature, saturation pressure (p_s), and water-vapor partial pressure (p_v) within the insulation layer of $\delta_{ins} = 100$ mm, for a vapor barrier layer of $\delta_4 = 16$ mm, and an external air temperature of $t_e = 40$ °C.

6.4. Influence of Wind Speed on the Exterior Surface of a Composite Wall

The outdoor convective heat transfer coefficient (h_e) at the wall's exterior surface was directly influenced by wind speed. Increasing h_e slightly increases the temperature and saturation vapor pressure in the insulation layer. By contrast, the vapor pressure remains practically unaffected (Tables 3–5). This indicates that external wind provides a protective effect against condensation within the insulation layer.

Table 3. Variation in t, p_s, p_v within the insulation layer for $\delta_{ins} = 100$ mm, $\delta_4 = 16$ mm, $\varphi_e = 0.85$, $t_e = 30$ °C and $h_e = 20$ W/(m^{2}K).

Intra Insulation Layer Thickness x [m]	$t_{intra_walls_ins}$ [°C]	$ps_{intra_walls_ins}$ [Pa]	$pv_{intra_walls_ins}$ [Pa]
0	19.14	2217	711.2
0.02	11.76	1381	594
0.04	4.375	835.3	476.7
0.06	−3.007	475.8	359.5
0.08	−10.39	251	242.3
0.1	−17.77	127.6	125

Table 4. Variation in t, p_s, p_v within the insulation layer for $\delta_{ins} = 100$ mm, $\delta_4 = 16$ mm, $\varphi_e = 0.85$, $t_e = 30$ °C and $h_e = 30$ W/(m^{2}K).

Intra Insulation Layer Thickness x [m]	$t_{intra_walls_ins}$ [°C]	$ps_{intra_walls_ins}$ [Pa]	$pv_{intra_walls_ins}$ [Pa]
0	19.33	2244	711.2
0.02	11.92	1395	594
0.04	4.496	842.4	476.7
0.06	−2.923	479.1	359.5
0.08	−10.34	252.1	242.3
0.1	−17.76	127.8	125

Table 5. Variation in t, p_s, p_v within the insulation layer for $\delta_{ins} = 100$ mm, $\delta_4 = 16$ mm, $\varphi_e = 0.85$, $t_e = 30\ ^\circ C$ and $h_e = 40\ W/(m^2K)$.

Intra Insulation Layer Thickness x [m]	$t_{intra_wall_ins}$ [°C]	$ps_{intra_wall_ins}$ [Pa]	$pv_{intra_wall_ins}$ [Pa]
0	19.43	2257	711.2
0.02	11.99	1402	594
0.04	4.557	846	476.7
0.06	−2.881	480.9	359.5
0.08	−10.32	252.7	242.3
0.1	−17.76	127.8	125

The insensitivity of p_v to changes in h_e is due to the neglect of convective resistance when calculating the molar diffusion flux (Equation (37)).

To assess the physical plausibility of the predicted fields, a literature-based benchmark against selected studies was performed. The comparison was restricted to quantities that are directly obtained from the present model and are sufficiently comparable across the selected studies, namely temperature in the compared wall zone, moisture-state indicators, and condensation occurrence. Because the present model directly yields water-vapor partial pressure and saturation pressure, an equivalent relative humidity, $RH_{eq} = \frac{p_v}{p_s}$, was derived where appropriate to facilitate comparison with studies reporting relative humidity; where other moisture indicators were reported in the literature (e.g., moisture content or vapor-pressure criterion), the comparison was retained at the level of the reported physical state. The resulting benchmark is summarized in Appendix A, Table A2.

Overall, the predicted ranges of wall-zone temperature and moisture-state indicators fall within the ranges reported in previous studies, supporting the adopted steady-state formulation within its intended scope. Direct literature data for molar vapor flux and time-dependent condensate accumulation are not reported in the selected studies and were therefore not used as benchmark quantities.

7. Conclusions

This paper applies a rigorous analogy between conductive heat transfer and diffusive moisture transport through the external wall of a refrigerated warehouse.

The physical mechanism leading to interstitial condensation in the insulation layer is explained, and a practical methodology is presented to identify (i) the insulation region where condensation is expected and (ii) the constructive measures required to mitigate this risk.

Based on the relative positions of the saturation and partial vapor pressure profiles, the location of condensation within the insulation layer can be determined. This paper provides calculation routines to evaluate the temperatures, water-vapor saturation pressures, and partial pressures at the wall inter-layer and within individual wall layers.

A parametric analysis quantifies the influence of the insulation thermal resistance and vapor barrier diffusion resistance on the condensation risk. For the investigated multilayer wall assembly, outdoor boundary conditions— especially outdoor relative humidity—strongly affected the condensation onset within the insulation. The effects of outdoor humidity, outdoor temperature, and wind speed were analyzed to support the design-oriented evaluation of cold-store wall assemblies.

The present results refer to the adopted steady-state operating conditions and to the assumption of constant wall-layer properties.

Future work will extend the present analysis to transient boundary conditions for the selected wall configuration.

Author Contributions: Conceptualization, L.M.C., L.G., T.C. and A.D.; methodology, D.T. and C.I.; software, L.M.C. and A.A.P.; validation, C.I. and D.T.; formal analysis, L.G. and T.C.; investigation, D.T. and A.A.P.; resources, C.I. and L.M.C.; data curation, C.I. and D.T.; writing—original draft preparation, L.M.C. and A.D.; writing—review and editing, L.G. and T.C.; visualization, A.A.P.; supervision, L.G. and A.D.; project administration, A.D.; funding acquisition, C.I. All authors have read and agreed to the published version of the manuscript.

Funding: This research was funded by the Romanian Ministry of Education and National University of Science and Technology Politehnica Bucharest through the PubArt Program.

Data Availability Statement: Data are contained within the article.

Conflicts of Interest: The authors declare no conflicts of interest.

Abbreviations

The following abbreviations are used in this manuscript:

EES	Engineering Equation Solver
HAM	Heat–Air–Moisture
HFM	Heat Flow Meter
RH	Relative Humidity
Latin Letters	
A	area normal to the heat/mass-transfer direction, [m^2]
a	thermal diffusivity, [$m^2 \cdot s^{-1}$]
$\bar{c}_i$	molar composition of component i in a mixture, [–]
c_p	specific heat at constant pressure, [$J \cdot kg^{-1} \cdot K^{-1}$]
D	molar diffusivity coefficient, [$m^2 \cdot s^{-1}$]
D_{AB}	molar diffusion coefficient of a component A through a medium B, [$m^2 \cdot s^{-1}$]
$\overline{G}$	unitary molar flux, [$kmol \cdot m^{-2} \cdot s^{-1}$]
h	convective heat transfer coefficient, [$W \cdot m^{-2} \cdot K^{-1}$]
$\bar{j}$	molar diffusion flux or molar diffusion velocity, [$kmol \cdot m^{-2} \cdot s^{-1}$]
k	thermal conductivity, [$W \cdot m^{-1} \cdot K^{-1}$]
M	molar mass, [$kg \cdot kmol^{-1}$]
N	amount of substance, [kmol]
n	coordinate normal to the isothermal surface/transfer direction, [m]
P,p	point, pressure, [Pa]
p_s	saturation pressure of water vapor, [Pa]
p_v	partial pressure of water vapor, [Pa]
q	unitary heat flux, [$W \cdot m^{-2}$]
R_D^{mol}	molar diffusion resistance, [$m^2 \cdot Pa \cdot s \cdot kmol^{-1}$]
R_t^{cond}	conduction thermal resistance, [$m^2 \cdot K \cdot W^{-1}$]
t	temperature, [°C]
T	absolute temperature, [K]
U	overall heat transfer coefficient, [$W \cdot m^{-2} \cdot K^{-1}$]
V	volume, [m^3]
w	velocity, [$m \cdot s^{-1}$]
x	coordinate through the wall thickness, [m]
Greek Symbol	
δ	layer thickness, [m]
$\overline{\mu}$	molar permeability coefficient, [$kmol \cdot m^{-1} \cdot s^{-1} \cdot Pa^{-1}$]
ρ	mass density, [$kg \cdot m^{-3}$]
$\overline{\rho}$	molar density, [$kmol \cdot m^{-3}$]
τ	time, [s]
φ	relative humidity coefficient, [–]

Subscripts

A	component A
D	diffusive
e	exterior/outdoor side
i	interior/indoor side, component
ins	insulation layer
inter-walls	between different layers of wall
intra-wall	inside a specific wall
intra_walls_ins	layer inside the insulation layer
j = 1, 2, . . ., 6	wall-layer numbering from exterior to interior
ma	moist air
v	water vapor
vw	vaporwall, of the water vapor through the wall

Appendix A

The calculation subroutines used are presented in Table A1.

Table A1. The subroutines employed for calculations.

Computed Parameter	EES Subprogram
$\sum \left(\frac{\delta}{k}\right)_j = \sum R_j^{cond}$	FUNCTION R_cond
Temperature inter-wall	PROCEDURE temp_inter_wall
Temperatura intra-wall	FUNCTION t_intra_wall
$\sum \left(\frac{\delta}{\overline{\mu}}\right)_j = \sum R_j^{dif}$	FUNCTION R_D
p_s inter-wall	PROCEDURE p_s_inter_wall
p_v inter-wall	PROCEDURE p_v_inter_wall
p_s intra-wall	FUNCTION p_s_intra_wall
p_v intra-wall	FUNCTION p_v_intra_wall
δ_{ins}	PROCEDURE insulation

```
FUNCTION R_cond(delta_1, k_1, delta_2, k_2, delta_3, k_3, delta_4, k_4, delta_6, k_6)
R_cond := (delta_1/k_1) + (delta_2/k_2) + (delta_3/k_3) + (delta_4/k_4) + (delta_6/k_6)
END

PROCEDURE temp_inter_wall(te, ti, U_r, h_e, h_i, R_cond_1, R_cond_2, R_cond_3, R_cond_4, R_cond_5: q, t_1, t_2, t_3, t_4, t_5, t_6, t_7)
q = U_r * (te − ti)
t_1 = te − q/h_e
t_2 = te − q * (1/h_e + R_cond_1)
t_3 = te − q * (1/h_e + R_cond_2)
t_4 = te − q * (1/h_e + R_cond_3)
t_5 = te − q * (1/h_e + R_cond_4)
t_6 = te − q * (1/h_e + R_cond_5)
t_7 = ti + q/h_i

END
FUNCTION t_intra_wall(t_in, t_fin, delta_wall, x)
t_intra_wall := (t_fin − t_in)/delta_wall * x + t_in
END

FUNCTION R_D(delta_1, mu_1, delta_2, mu_2, delta_3, mu_3, delta_4, mu_4, delta_ins_chosen, mu_ins, delta_6, mu_6)
R_D := (delta_1/mu_1) + (delta_2/mu_2) + (delta_3/mu_3) + (delta_4/mu_4) + (delta_ins_chosen/mu_ins) + (delta_6/mu_6)
```

```
END

PROCEDURE p_s_inter_wall(t_1, t_2, t_3, t_4, t_5, t_6, t_7: p_s_1, p_s_2, p_s_3, p_s_4,
p_s_5, p_s_6, p_s_7)
p_s_1 = P_sat(Water, T = T_1)
p_s_2 = P_sat(Water, T = T_2)
p_s_3 = P_sat(Water, T = T_3)
p_s_4 = P_sat(Water, T = T_4)
p_s_5 = P_sat(Water, T = T_5)
p_s_6 = P_sat(Water, T = T_6)
p_s_7 = P_sat(Water, T = T_7)
END

PROCEDURE p_v_inter_wall(p_v_e, p_v_i, R_D_1, R_D_2, R_D_3, R_D_4, R_D_5, R_D_6:
w, p_v_1, p_v_2, p_v_3, p_v_4, p_v_5, p_v_6, p_v_7)
w = (p_v_e-p_v_i)/R_D_6
p_v_1 = p_v_e
p_v_2 = p_v_e-w * R_D_1
p_v_3 = p_v_e-w * R_D_2
p_v_4 = p_v_e-w * R_D_3
p_v_5 = p_v_e-w * R_D_4
p_v_6 = p_v_e-w * R_D_5
p_v_7 = p_v_e-w * R_D_6
END

FUNCTION p_s_intra_wall(t_in, q, x, k)
t = t_in − q * x/k
p_s_intra_wall := P_sat(water, T = t)
END

FUNCTION p_v_intra_wall(p_v_in, w, x, mu)
p_v_intra_wall := p_v_in − w * x/mu
END

PROCEDURE Insulation(k_ins, h_e, h_i, R, U_est, te, tr, ti, m: delta_ins_c, delta_ins_chosen,
U_r, U_s, N)
delta_ins_c = k_ins * ((1/U_est) − ((1/h_e) + R + (1/h_i)))
IF (delta_ins_c > 0.03) AND (delta_ins_c < 0.065) THEN delta_ins_chosen := 0.06
IF (delta_ins_c > 0.065) AND (delta_ins_c < 0.083) THEN delta_ins_chosen := 0.08
IF (delta_ins_c > 0.083) AND (delta_ins_c < 0.104) THEN delta_ins_chosen := 0.10
IF (delta_ins_c > 0.104) AND (delta_ins_c < 0.110) THEN delta_ins_chosen := 0.12
IF (delta_ins_c > 0.110) AND (delta_ins_c < 0.139) THEN delta_ins_chosen := 0.14
IF (delta_ins_c > 0.140) AND (delta_ins_c < 0.199) THEN delta_ins_chosen := 0.16
IF (delta_ins_c > 0.200) AND (delta_ins_c < 0.249) THEN delta_ins_chosen := 0.18
U_r = 1/((1/h_e) + R + (1/h_i) + (delta_ins_chosen/k_ins))
U_s = 0.95 * ((te − tr)/(te − ti)) * (1/m) * alpha_e
IF (U_s > U_r) THEN N := 0 ELSE N := 1
END
```

Table A2 provides a literature-based benchmark of the present model against published wall-scale hygrothermal studies, using aligned temperature, moisture-state, and condensation-related quantities.

Table A2. Literature-based benchmark for the present steady-state wall model.

Compared Wall Zone	Temperature	Moisture-Related Quantity	Physical Interpretation	Consistency with Present Model	Source
Near-exterior zone of a multilayer envelope in a transient HAM simulation (profiles reported over the outer part of the wall)	Temperature profile: ≈20–28 °C, in the reported near-exterior/mid-height wall zone, with lower temperatures in the coupled HAM case than in the heat-only case	RH ≈ 50–75% and vapor pressure across the plotted sections ≈ 2.20–2.65 kPa, increasing with time	Moisture ingress increases RH with time; away from the exposed outer surface, condensation/evaporation is required to satisfy local vapor balance. Coupled moisture transfer lowers local temperature relative to heat transfer alone.	Qualitative	[6]
Insulation–structure interface, point P2, rock-wool-board wall; winter 10-day monitoring	Interface temperature: cool winter interface, ≈9–12 °C at P2	Moisture content at P2 ≈1.6–2.1%	Even the least damaged wall retained measurable moisture at the interface; across the monitored walls, higher moisture content was associated with lower interface temperature	Partial	[10]
Critical condensation plane in a wall section assessed by the Glaser method	Not reported at the plane; critical months occurred under outdoor monthly means of ≈4–5 °C, with RH up to ≈87–89% in the future scenarios	saturation pressure $p_s \approx 0.836$–0.898 kPa; vapor-pressure line $p_v \approx 0.722$–0.794 kPa, with monthly condensate $\approx$ 0.0195–0.0359 $\frac{kg}{m^2}$	A wall that is non-condensing in the historical climate becomes seasonally condensing in future MPI/GFDL scenarios once vapor pressure exceeds the local saturation threshold. The condensate mass remains below the 1 kg m^{-2} criterion, but condensation onset is explicit.	Consistent	[11]
Insulation layer of the refrigerated-wall assembly (100 mm case; warm side to cold side)	Insulation temperature: decreases from ≈19.1–19.4 °C at the warm face to ≈−17.8 °C at the cold face	saturation pressure at the warm face: $p_s \approx 2.22$–2.26 kPa, with vapor-pressure $p_v \approx 0.711$ kPa. At the cold face: $p_s \approx 0.128$ kPa and $p_v \approx 0.125$ kPa; derived RH = p_v/p_s rises from ≈32% to ≈96–98%	Strong cooling through the insulation drives the cold-side region close to saturation; in parametric cases, condensation occurs when the local vapor pressure reaches or exceeds the saturation pressure	Reference	present study

References

1. Ali, A.; Issa, A.; Elshaer, A. A Comprehensive Review and Recent Trends in Thermal Insulation Materials for Energy Conservation in Buildings. *Sustainability* **2024**, *16*, 8782. [CrossRef]
2. International Energy Agency (IEA). Buildings. Available online: https://www.iea.org/energy-system/buildings (accessed on 11 January 2026).
3. Paraschiv, S.; Paraschiv, L.S.; Serban, A. Increasing the Energy Efficiency of a Building by Thermal Insulation to Reduce the Thermal Load of the Micro-Combined Cooling, Heating and Power System. *Energy Rep.* **2021**, *7*, 286–298. [CrossRef]
4. Lee, H.; Ozaki, A.; Lee, M.; Yamamoto, T. Humidity Control Effect of Vapor-permeable Walls Employing Hygroscopic Insulation Material. *Indoor Air* **2020**, *30*, 346–360. [CrossRef]
5. Zhou, S.; Ding, Y.; Wang, Z.; Dong, J.; She, A.; Wei, Y.; Li, R. Weathering of Roofing Insulation Materials under Multi-Field Coupling Conditions. *Materials* **2019**, *12*, 3348. [CrossRef] [PubMed]
6. Liu, F.; Jia, B.; Chen, B.; Geng, W. Moisture Transfer in Building Envelope and Influence on Heat Transfer. *Procedia Eng.* **2017**, *205*, 3654–3661. [CrossRef]
7. Künzel, H.M. Long-Term Thermal Performance of Insulations under Moisture Loads. In *Thermal Insulation and Radiation Control Technologies for Buildings*; Kośny, J., Yarbrough, D.W., Eds.; Green Energy and Technology; Springer International Publishing: Cham, Switzerland, 2022; pp. 37–53.

8. Khoukhi, M.; Hassan, A.; Al Saadi, S.; Abdelbaqi, S. A Dynamic Thermal Response on Thermal Conductivity at Different Temperature and Moisture Levels of EPS Insulation. *Case Stud. Therm. Eng.* **2019**, *14*, 100481. [CrossRef]
9. Jerman, M.; Černý, R. Effect of Moisture Content on Heat and Moisture Transport and Storage Properties of Thermal Insulation Materials. *Energy Build.* **2012**, *53*, 39–46. [CrossRef]
10. Wang, Y.; Wang, Q.; Chen, R.; Zhang, C.; Song, J. Comparative Analysis on Heat and Moisture Transfer of Composite Insulation Walls. *Int. J. Low-Carbon Technol.* **2024**, *19*, 2108–2118. [CrossRef]
11. Saricioglu, P.; Aycam, İ.; Harputlugil, G.U. Analysis of Condensation Risk in a Wall Section in the Context of Climate Change Scenarios. *Civ. Eng. Archit.* **2024**, *12*, 2159–2180. [CrossRef]
12. Budaiwi, I.; Abdou, A. The Impact of Thermal Conductivity Change of Moist Fibrous Insulation on Energy Performance of Buildings under Hot–Humid Conditions. *Energy Build.* **2013**, *60*, 388–399. [CrossRef]
13. Nagy, B.; Simon, T.K.; Nemes, R. Effect of Built-in Mineral Wool Insulations Durability on Its Thermal and Mechanical Performance. *J. Therm. Anal. Calorim.* **2020**, *139*, 169–181. [CrossRef]
14. Nosrati, R.H.; Berardi, U. Hygrothermal Characteristics of Aerogel-Enhanced Insulating Materials under Different Humidity and Temperature Conditions. *Energy Build.* **2018**, *158*, 698–711. [CrossRef]
15. El Assaad, M.; Plantec, Y.; Colinart, T.; Lecompte, T. Influence of Moisture Transfer on Thermal Conductivity Measurement by HFM: Measurement Accuracy on Insulation Materials and Consequences on Building Energy Assessments. *Energy Build.* **2024**, *320*, 114635. [CrossRef]
16. El Assaad, M.; Colinart, T.; Lecompte, T. Thermal Conductivity Assessment of Moist Building Insulation Material Using a Heat Flow Meter Apparatus. *Build. Environ.* **2023**, *234*, 110184. [CrossRef]
17. Florez, D.; Perré, P.; Segovia, C.; Rémond, R. Computational Characterisation of the Heat Flow Meter Method Applied to Moist Bio-Based Insulating Building Materials. *Int. J. Therm. Sci.* **2024**, *201*, 109038. [CrossRef]
18. Zhang, L.; Liu, Z.; Hou, C.; Hou, J.; Wei, D.; Hou, Y. Optimization Analysis of Thermal Insulation Layer Attributes of Building Envelope Exterior Wall Based on DeST and Life Cycle Economic Evaluation. *Case Stud. Therm. Eng.* **2019**, *14*, 100410. [CrossRef]
19. Omle, I.; Askar, A.H.; Kovács, E. Optimizing the Design of Container House Walls Using Argon and Recycled Plastic Materials. *Buildings* **2024**, *14*, 3944. [CrossRef]
20. Omle, I.; Kovács, E.; Bolló, B. Applying Recent Efficient Numerical Methods for Long-Term Simulations of Heat Transfer in Walls to Optimize Thermal Insulation. *Results Eng.* **2023**, *20*, 101476. [CrossRef]
21. BAUKLIMATIK Dresden. Bauklimatik Dresden Software. Available online: https://bauklimatik-dresden.de/en/ (accessed on 11 January 2026).
22. WUFI®. Available online: https://wufi.de/en/ (accessed on 11 January 2026).
23. Palani, H.; Tang, M.; Zhang, R.; Desjarlais, A. Assessing the Hygrothermal Performance of Bio-Based Materials in Building Wall Systems. *Constr. Build. Mater.* **2025**, *492*, 142907. [CrossRef]
24. Asphaug, S.K.; Time, B.; Kvande, T. Hygrothermal Simulations of Thermally Insulated Basement Envelopes-Importance of Boundary Conditions below Grade. *Build. Environ.* **2021**, *199*, 107920. [CrossRef]
25. Alsaad, H.; Hartmann, M.; Voelker, C. Hygrothermal Simulation Data of a Living Wall System for Decentralized Greywater Treatment. *Data Brief* **2022**, *40*, 107741. [CrossRef] [PubMed]
26. Liu, M.; Huang, L.; Wang, J. Hygrothermal Performance of Exterior Wall Assemblies Under Wind-Driven Rain Across China's Thermal Zones. *Buildings* **2025**, *15*, 4198. [CrossRef]
27. Hejazi, B.; Rodrigues Marques Sakiyama, N.; Frick, J.; Garrecht, H. Hygrothermal Simulations Comparative Study: Assessment of Different Materials Using WUFI and DELPHIN Software. In Proceedings of the 16th IBPSA Conference, Rome, Italy, 2–4 September 2019; pp. 4674–4681. [CrossRef]
28. Defo, M.; Lacasse, M.; Laouadi, A. A Comparison of Hygrothermal Simulation Results Derived from Four Simulation Tools. *J. Build. Phys.* **2022**, *45*, 432–456. [CrossRef]
29. *DIN 4108-3:2018-10*; Thermal Protection and Energy Economy in Buildings-Part 3: Protection against Moisture Subject to Climate Conditions-Requirements, Calculation Methods and Directions for Planning and Construction. German Institute for Standardisation (Deutsches Institut für Normung): Berlin, Germany, 2018.
30. *ISO 13788:2013*; Hygrothermal Performance of Building Components and Building Elements—Internal Surface Temperature to Avoid Critical Surface Humidity and Interstitial Condensation—Calculation Methods. International Organization for Standardization (ISO): Geneva, Switzerland, 2012.
31. Klein, S.A. *Engineering Equation Solve*, 64-bit Academic Professional V10.836-3D; F-Chart: Madison, WI, USA, 2020.

32. Won, Y.-Y.; Ramkrishna, D. Revised Formulation of Fick's, Fourier's, and Newton's Laws for Spatially Varying Linear Transport Coefficients. *ACS Omega* **2019**, *4*, 11215–11222. [CrossRef]
33. Porneala, S.; Porneala, D. *Refrigeration and Air Conditioning Systems in the Food Industry*; ALMA Publishing House: Galați, Romania, 1997.

Disclaimer/Publisher's Note: The statements, opinions and data contained in all publications are solely those of the individual author(s) and contributor(s) and not of MDPI and/or the editor(s). MDPI and/or the editor(s) disclaim responsibility for any injury to people or property resulting from any ideas, methods, instructions or products referred to in the content.